Journal of Asian Earth Sciences 284 (2025) 106540

Contents lists available at ScienceDirect

Journal of Asian Earth Sciences

journal homepage: www.elsevier.com/locate/jseaes

Present-day geothermal regime of the Junggar Basin, northwest China: Implication for hydrocarbon distribution and geothermal resources

Chenxing Li [a,b], Jian Chang [a,b,*], Nansheng Qiu [a,b,*], Huajun Guo [c], Xiang Shan [c], Bo Peng [c], Jiabo Xu [a,b], Ze Zhang [a,b]

[a] State Key Laboratory of Petroleum Resources and Engineering, China University of Petroleum (Beijing), Beijing 102249, China
[b] College of Geosciences, China University of Petroleum (Beijing), Beijing 102249, China
[c] PetroChina Hangzhou Research Institute of Geology, Hangzhou 310023, China

ARTICLE INFO

Keywords:
Junggar Basin
Geothermal regime
Deep formation temperature
Hydrocarbon generation
Geothermal resources

ABSTRACT

The geothermal regime not only reflects the basin's evolutionary history but also controls the formation of both fossil energy and geothermal resources. The deep geothermal characteristics of the Junggar Basin in northwestern China have remained unclear due to limited temperature data. In this study, we collected new temperature data from over 450 boreholes drilled in the past decade to investigate the geothermal gradient, heat flow, formation temperatures at depths of 5 to 10 km, and the thermal structure of lithosphere. The results show that the geothermal gradient ranges from 14.0 to 29.8°C/km, with an average of 20.7°C/km, and heat flow ranges from 32.7 and 68.5 mW/m^2, averaging 45.8 mW/m^2. Heat flow varies between uplifts and depressions, influenced by basement relief, with further regional variation in the north and south due to basement lithology and faults. The ratio of crust to mantle heat flow and the thermal lithosphere thickness across different tectonic units ranges from 0.74 to 1.92 and 150 to 270 km, respectively, confirming the basin's stable tectonic background. Formation temperatures at 10 km depth ranges from 155°C to 311°C, increasing from the center to the basin's margins. These findings suggest that oil can be found at depths of 8000 m in the Central Depression, while high-temperature geothermal resources are present around 5000 m in the Eastern Uplift. This study provides a comprehensive understanding of the geothermal regime and valuable insights for future resource exploration in the Junggar Basin.

1. Introduction

Recent advancements in drilling technology and exploration activities have facilitated the identification of new hydrocarbon development targets in the deep formations of basins such as the Junggar, Sichuan, and Tarim Basins in China (Gu et al., 2019; Jia and Pang, 2015). These explorations have revealed that liquid oil still exists at depths exceeding 7000 m in the Junggar Basin; however, the ambient temperature of these hydrocarbon-bearing environments remains understudied (He et al., 2019). Notably, geothermal characteristics play a crucial role in determining the distribution of hydrocarbon and geothermal resources. Therefore, a comprehensive understanding of the geothermal regime is not only essential for effective oil and gas exploration but also vital for the assessing geothermal resources.

Previous studies of geothermal characteristics on the Junggar Basin have identified it as a "cold basin" with low geothermal gradients and heat flow (Jin et al., 2021; Qiu et al., 2001; Rao et al., 2013; Wang et al., 2000, Zhang et al., 2024). Early research by Wang et al. (2000, 2001) highlighted that terrestrial heat flow is higher in the uplifted areas and lower in the depressed. Qiu et al. (2001) found that the geothermal gradient is highest in the eastern region, lower in the northwestern and northern regions, and lowest in the south. Rao et al. (2013) similarly noted that heat flow peaks in the east, with lower values in the central and southern regions. Recent studies by Zhang et al. (2024) confirmed these patterns, with an average geothermal gradient of 20.9°C/km and a heat flow of 45.1 mW/m^2. However, early oil and gas exploration focused primarily on the basin's uplifts, leading to discrepancies in the geothermal characteristics due to the uneven distribution of boreholes. As more borehole data from the basin's central and marginal areas become available, a clearer picture of the geothermal distribution is emerging (Zhang et al., 2024). With the increasing volume of temperature data, attention has shifted to temperature anomalies caused by

* Corresponding authors at: State Key Laboratory of Petroleum Resources and Engineering, China University of Petroleum (Beijing), Beijing 102249, China.
E-mail addresses: changjian@cup.edu.cn (J. Chang), qiunsh@cup.edu.cn (N. Qiu).

https://doi.org/10.1016/j.jseaes.2025.106540
Received 8 October 2024; Received in revised form 14 February 2025; Accepted 2 March 2025
Available online 4 March 2025

groundwater circulation and faulting, necessitating further investigation of localized geothermal influences (Jin et al., 2021).

Formation temperature is another critical aspect of geothermal studies. Previous research focused mainly on formations at depths of 3000–6000 m, revealing temperatures between 140℃ and 160℃ at 6000 m (Qiu et al., 2001). However, the lack of temperature data for formations deeper than 6000 m remains a key barrier to ultra-deep oil, gas, and geothermal resource exploration. Additionally, understanding the lithospheric thermal structure is essential for basin dynamics (Zhi et al., 2018), though most studies in the Junggar Basin have concentrated on the Eastern Uplift and Southern Overthrust Belt (Rao et al., 2013). As a result, comprehensive studies on the lithospheric thermal structure and crust-mantle heat flow across different structural units of the basin are still lacking.

In this study, we integrated new borehole temperature data from over the past decade with measured rock thermal properties to analyze geothermal parameters, including geothermal gradient, heat flow, formation temperatures of depths of 5000–10000 m, and the lithosphere thermal structure o across various structural units of the Junggar Basin. We also examined factors influencing the geothermal distribution, concluding that groundwater circulation affects the geothermal gradient on the northwestern margin, while faulting contributes to temperature anomalies on the southern margin. Based on these studies, we predict the oil and gas phase state at deep formations and identify the depth of high-temperature geothermal resources in the basin, providing crucial insights for sustainable resource exploration and development.

2. Geological setting

The Junggar Basin, renowned for its abundant hydrocarbon resources, is in the Central Asian Orogenic Belt (Fig. 1a). It is bordered by the Zhayier and Halaalate Mountains to the west, the Qinggelidi and Delun Mountains to the north, the Bogeda and Yilinheibiergen Mountains to the south, and the Kelameili Mountains to the east (He et al., 2018). The basin has a triangular shape, extending 700 km east–west and 370 km north–south, covering an area of approximately 13.4 × 10^4 km^2. It consists of 6 major tectonic units— the Central Depression, Western Uplift, Luliang Uplift, Wulungu Depression, Southern Overthrust Belt, and Eastern Uplift— further subdivided into 44 secondary tectonic units (Fig. 1b; Wu et al., 2022).

The basin's evolution has included several phases: basin formation and transition during the Carboniferous to Permian, lacustrine deposition in the Mesozoic to Paleogene, and intense compression from the Neogene to Quaternary (Fig. 1c, d, Fig. 2; Guan et al., 2024). The Carboniferous and Lower Permian are primarily volcanic, while the Middle Permian formations consist mainly of fine-grained sandstones in a lacustrine environment. Upper Permian deposits include coarse-grained sedimentary rocks. From the Lower to Middle Triassic, lacustrine and fan delta environments prevailed, transitioning to lacustrine in the Upper Triassic. During the Jurassic, the sedimentary environment shifted to limnetic facies, and by the Lower Cretaceous, fluvial-lacustrine facies dominated the basin, continuing into the Paleogene (Zhou et al., 2024). The Neogene to Quaternary period saw the deposition of conglomerates (Fig. 2; He et al., 2005, 2018).

The basin's multi-phase tectonic evolution has generated various source rocks, including Carboniferous, Middle and Lower Permian, and Jurassic, along with associated reservoir and caprock combinations, creating multiple superimposed hydrocarbon systems (He et al., 2018, 2019). These tectonic events have also resulted in complex structural variations and unconformities (Fig. 2), causing significant differences in the depth and distribution of formations across the basin (Fig. 1c, d). Notably, southward subsidence and northward uplift since the Cretaceous have created the current wedgelike structure, leading to pronounced differences in the distribution of deep formations and formation temperatures across the basin's tectonic units (Fang et al., 2006).

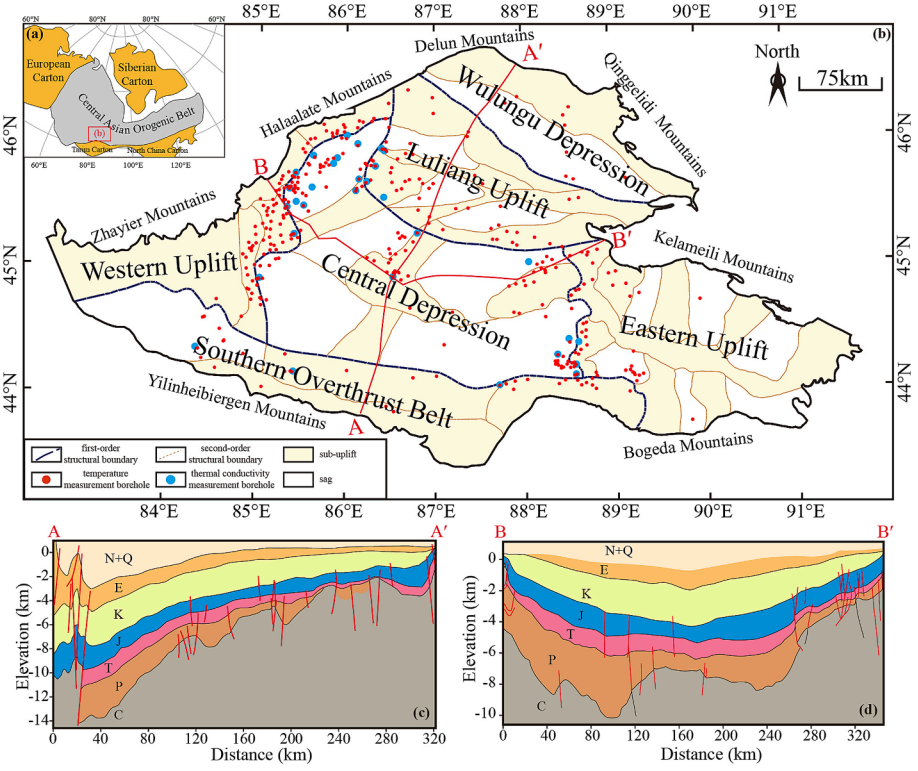

Fig. 1. (a) Simplified distribution map of the tectonic units in China. (b) Tectonic units map of the Junggar Basin (Wang et al., 2001). (c) South-north geological cross section A-A'; (d) West-east geological cross section B-B'.

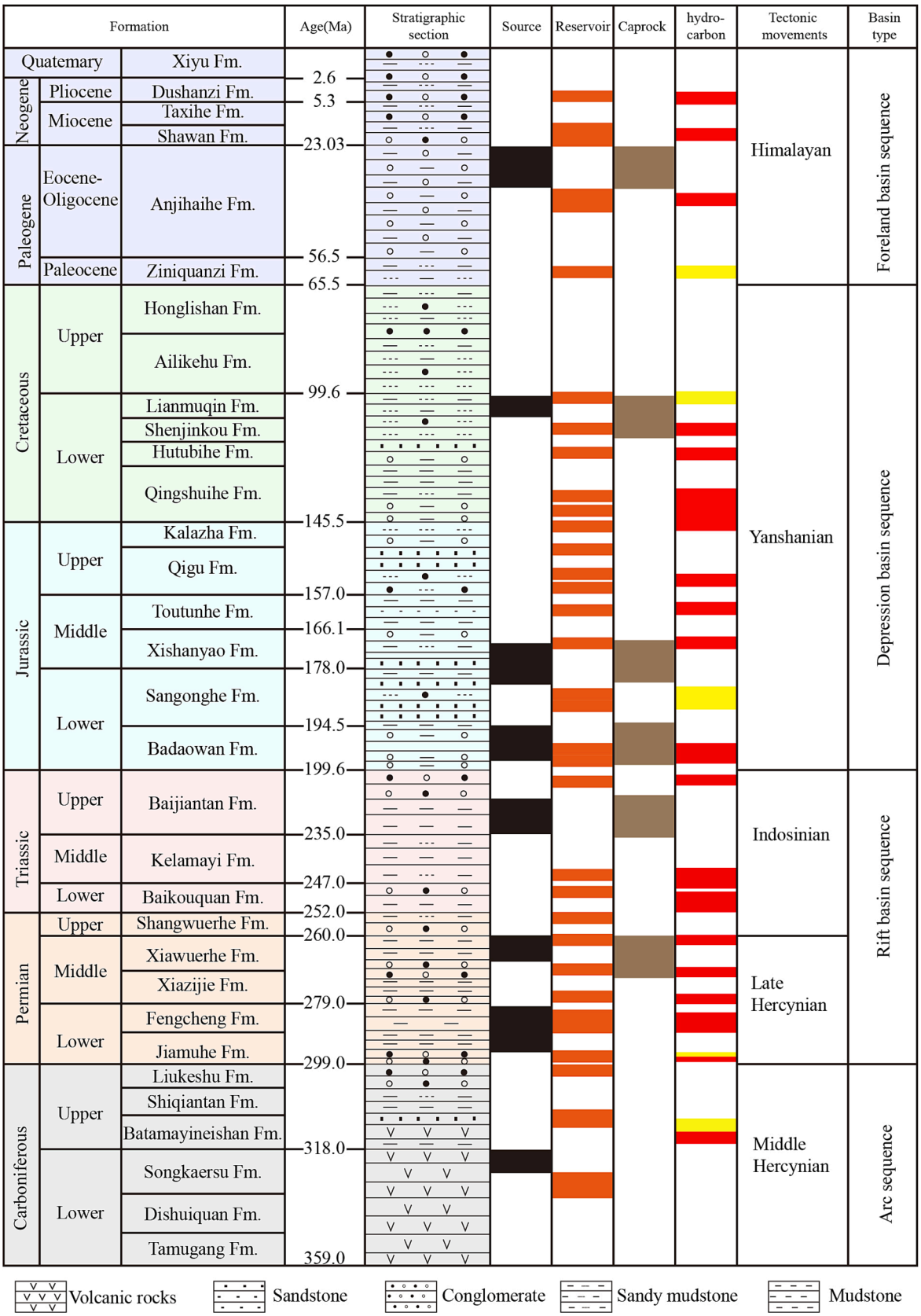

Fig. 2. Stratigraphy of the Junggar Basin (modified from the Xinjiang Oilfield Company).

3. Geothermal characteristics

3.1. Thermal properties of rocks

Thermal conductivity is a rock property that measures the rate of heat transfer through a unit area per unit of time when there is a 1℃ temperature gradient over a unit length in the direction of heat flow. It is essential for calculating geothermal parameters. Common methods for measuring thermal conductivity include the one-dimensional steady-state heat source method, optical scanning method and transient plane heat source method (Kämmlein and Stollhofen, 2019; Popov et al., 1999).

In this study, thermal conductivity was measured for 98 rock samples from 30 boreholes located in the Luliang Uplift, Southern Overthrust Belt and Central Depression (Fig. 1b). These samples, spanning formations from the Carboniferous to the Neogene, include sandstone, mudstone, conglomerate, and volcanic rocks. Prior to testing, rock samples were vacuum-saturated to fully hydrate their pores, ensuring results that closely reflect in-situ conditions (Song et al., 2023). The tests were conducted using a German-made TCS (Thermal Conductivity Scanning) automatic thermal conductivity scanner.

The thermal conductivity of the 98 samples ranged from 1.60 to 3.72 W/(m·K), with an average of 2.48 ± 0.41 W/(m·K) (Fig. 3a). Conglomerates exhibited the highest conductivity, averaging 2.68 ± 0.38 W/(m·K), followed by sandstones (2.56 ± 0.38 W/(m·K)) and volcanic rocks (2.32 ± 0.54 W/(m·K)). Mudstones had the lowest values, averaging 2.27 ± 0.32 W/(m·K) (Table 1).Correlation charts (Fig. 3b) show that thermal conductivity generally increases with depth, consistent with the principle that compaction enhances thermal conductivity. However, the rate of increase varies by lithology. Sandstone and conglomerates, with higher porosity, experience rapid pore compaction with depth, leading to a marked decrease in thermal conductivity. In contrast, mudstone and volcanic rocks, which have lower porosity, show only modest increase.

To derive representative thermal conductivity values for each formation, the harmonic mean of thermal conductivity was calculated using the data from these 98 samples, along with published values for 347 other rock samples (Table 2). Statistical analysis indicates that Triassic rocks have the highest thermal conductivity at 2.47 W/(m·K), followed by Jurassic (2.27 W/(m·K)) and Carboniferous (2.26 W/(m·K)) rocks. Permian rocks have a conductivity of 2.18 W/(m·K), while Cretaceous, Paleogene, and Neogene strata show lower conductivities, ranging from 1.73 to 1.91 W/(m·K). By combining these thermal conductivity values with the thicknesses of the formations in the temperature measurement boreholes, we can calculate the mean thermal conductivity for each borehole (Chang et al., 2016).

Table 1
Thermal conductivity data of different lithology in the Junggar Basin.

lithology	depth range (m)	number of samples	thermal conductivity range (W/(m·K))	average ± standard division (W/(m·K))
Sandstone	1189 ~ 6542	38	1.934 ~ 3.483	2.552 ± 0.373
Mudstone	1964 ~ 6152	28	1.757 ~ 3.132	2.269 ± 0.321
Conglomerate	1865 ~ 5973	23	2.001 ~ 3.715	2.679 ± 0.376
Volcanic	2979 ~ 6994	9	1.603 ~ 3.447	2.318 ± 0.544

3.2. Borehole temperature profiles

Geothermal geological research largely relies on borehole temperature data, but the quality of these datasets can vary due to differences in measurement methods. Four common techniques for obtaining borehole temperatures are oil testing, steady-state measurement, bottom-hole testing and drill-stem testing, each serving a unique role in geothermal analysis. (Qiu et al., 2001).

Steady-state temperature refers to measurements taken after the formation temperature has reached thermal equilibrium. This method involves continuous temperature readings taken at depths ranging from deep to shallow at 50–100 m intervals, making it the most accurate and representative of the region's temperature profile. In this study, steady-state temperature data from 141 new boreholes across all first-order structural units, except the Wulungu Depression, were collected. The R-squared (r^2) value exceeds 0.99 for individual boreholes and is 0.969 for the entire dataset, confirming a strong linear correlation between formation temperature and depth under steady-state conditions (Fig. 4).

Due to the limited availability and uneven distribution of steady-state data, oil testing temperature data from over 300 boreholes were also used to enhance our understanding of the geothermal characteristics in the Junggar Basin (Fig. 5). Oil testing measures the formation temperature recorded after placing an instrument in the perforated interval following a period of borehole closure, ranging from several days to weeks. These measurements are crucial for geothermal studies. The oil testing data in this study covers all tectonic units of the Junggar Basin, with depths from 300 to 7300 m, extending deeper than the steady-state data. The R-squared of oil testing data is 0.897, and the curve fitting slope is 0.2, corresponding to a geothermal gradient of 20℃/km, which is lower than the 22℃/km observed in the steady-state data. Accurate geothermal gradient must be assessed based on borehole locations, which will be discussed in the following section.

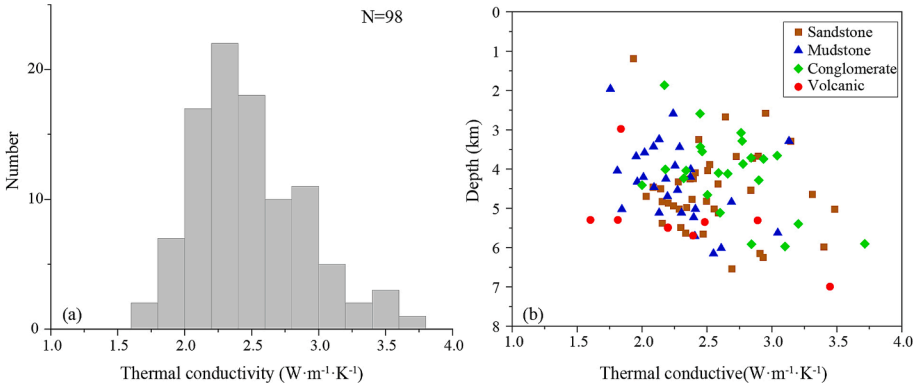

Fig. 3. Histogram of thermal conductivity in Junggar Basin (a) and the relationship between thermal conductivity and depth by different lithologies in the Junggar Basin (b).

Table 2
Thermal conductivity data of different strata in the Junggar Basin.

Stratum	Lithology	Number of samples	Ranges(W/(m·K))	Average thermal conductivity ± standard deviation(W/(m·K))	Harmonic mean thermal conductivity(W/(m·K))
N	Sandstone	1	3.483	3.483	1.855
		7		1.695 [a]	
		1		2.295[b]	
E	Sandstone	2	2.771–3.145	3.016 ± 0.213	1.908
	Mudstone	1	3.132	3.132	
		3		1.581 [a]	
		8		1.794[b]	
K	Sandstone	1	2.555	2.555	1.723
	Conglomerate	3	2.173 ~ 3.715	2.911 ± 0.774	
	Mudstone	1	2.411	2.411	
		20		1.462 [a]	
		28		1.837[b]	
J	Sandstone	5	1.934 ~ 2.951	2.616 ± 0.433	2.271
	Mudstone	4	1.757 ~ 2.550	2.170 ± 0.328	
	Conglomerate	1	2.447	2.447	
		57		2.187 [a]	
		101		2.307[b]	
T	Sandstone	8	2.286 ~ 3.400	2.827 ± 0.378	2.471
	Mudstone	4	1.845 ~ 2.290	2.091 ± 0.226	
	Conglomerate	6	2.504 ~ 2.936	2.747 ± 0.15	
		15		2.303 [a]	
		15		2.505[b]	
P	Sandstone	22	2.032 ~ 2.932	2.369 ± 0.214	2.178
	Mudstone	18	1.810 ~ 3.045	2.291 ± 0.296	
	Conglomerate	12	2.001 ~ 3.203	2.599 ± 0.384	
	Andesite	1	1.603	1.603	
	Tuff	1	1.814	1.814	
		43		1.993 [a]	
		23		2.176[b]	
C	Tuff	1	3.447	3.447	2.255
	Andesite	4	1.837–2.890	2.401 ± 0.434	
	Basalt	2	2.199–2.200	2.200 ± 0.001	
		15		2.202 [a]	
		11		2.218[b]	

Note: a: Qiu et al., 2001; b: Rao et al., 2013.

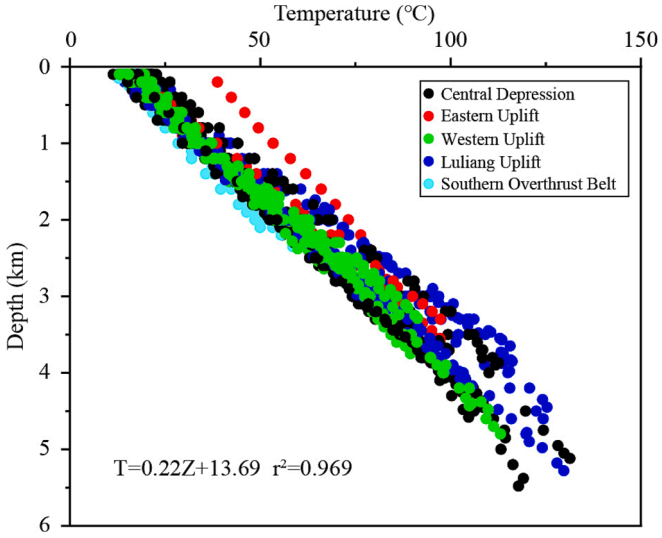

Fig. 4. The borehole temperature data of steady-state measurement; T is the formation temperature and Z is the corresponding depth; r^2 is the R-squared coefficient.

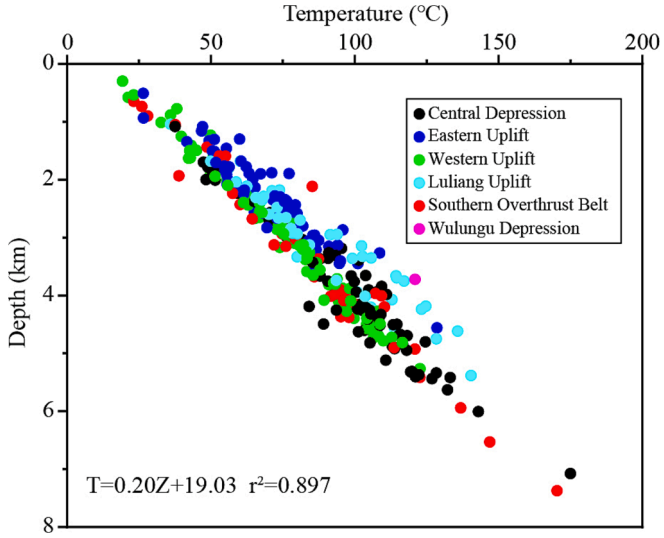

Fig. 5. The borehole temperature data of oil testing; T is the formation temperature and Z is the corresponding depth; r^2 is the R-squared coefficient.

3.3. *The geothermal gradient and heat flow*

Statistical analysis of geothermal gradients at different depths reveals minimal variation 3000 m, followed by a significant decrease below 3000 m (Fig. 6). This pattern supports the idea that geothermal gradient variation is influenced by thermal conductivity, which is affected by lithology and compaction. To avoid potential misinterpretation from comparing geothermal gradients across different depths in regional lateral comparisons, we standardized the analysis to a depth section of depth section of 0–4000 m for selected boreholes. This calculation used experimentally measured thermal conductivity and applied the one-dimensional heat conduction equation (Equation (1) to derive temperatures at a uniform depth.

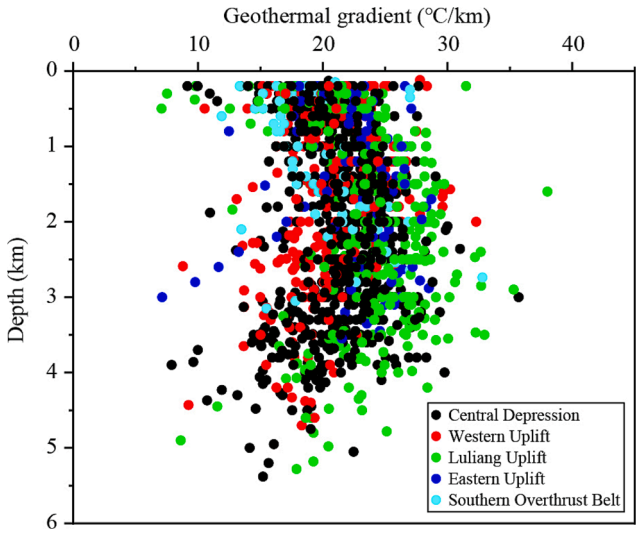

Fig. 6. The relationship between geothermal gradient and depth in the Junggar Basin.

$$T_i^b = T_i^t + \frac{(q_i^t \times Z_i)}{K_i} - \frac{(A_i \times Z_i^2)}{(2 \times K_i)} \quad (1)$$

Where T_i^b is the formation bottom temperature (℃), T_i^t is the formation top temperature (℃), A_i is the radioactive heat production rate (μW/m^3), q_i^t serve as the top heat flow (mW/m^2), K_i is the thermal conductivity (W/(m·K)), and Z_i is the formation thickness (km).

Subsequently, geothermal gradients were calculated using the gradient equation (Equation (2) at the 0–4000 m depth section.

$$G_{4000} = \frac{(T_{4000} - T_0)}{(Z_{4000} - Z_0)} \quad (2)$$

Where G_{4000} represents the geothermal gradient (℃/km); T_{4000} is the calculated temperature (℃); Z_{4000} is the unified depth 4000 m; T_0 and Z_0 are the temperature and depth of constant temperature zone (14 ℃ and 20 m in the Junggar Basin).

To address gaps in data coverage, kriging interpolation was applied to geothermal gradient data from over 450 boreholes, resulting in a detailed planar distribution map of geothermal gradients at the 0–4000 m depth across the basin. The analysis revealed geothermal gradients ranging from 14.0 to 29.8℃/km, with an average of 20.7℃/km for the Junggar Basin (Fig. 7). Specifically, the Central Depression and the southern margin of the basin exhibited lower geothermal gradients, ranging from 17.2 to 28.1℃/km and 16.5 to 23.7℃/km, with average values of 20.1℃/km and 20.0℃/km, respectively. In contrast, the Western Uplift and the Wulungu Depression exhibited intermediate geothermal gradients, ranging from 14.1 to 24.7 ℃/km and 16.3 to 25.5 ℃/km, with average values of 20.9 ℃/km and 20.8 ℃/km, respectively. Additionally, the Luliang Uplift and the Eastern Uplift were featured by higher geothermal gradients, ranging from 15.4 to 29.5℃/km and 17.3 to 29.8 ℃/km, averaging 21.1℃/km and 21.5℃/km, respectively (Fig. 7).

Our findings, incorporating a broader dataset, show that the basin's average geothermal gradient is slightly lower than the 20.9℃/km reported by Zhang et al. (2024). This difference is due to our use of a standardized depth of 4000 m, which provides a more consistent comparison across structural units. When compared to other basins in China, the geothermal gradient of the Junggar Basin is more similar to that of the Tarim Basin (23℃/km). However, it is lower than that of the Ordos Basin (29.3℃/km) and the Bohai Bay (30–36℃/km) observed in the Bohai Bay Basin in eastern China (Chang et al., 2016; Ren et al., 2007). Notably, our study identified an increase in the geothermal gradient near the piedmont areas of the southern margin, challenging previous research that suggested this region had a lower gradient than the Central Depression. By incorporating additional drilling data from the basin's periphery, we offer a more accurate assessment of the region's geothermal gradient.

Additionally, surface heat flow was estimated for all borehole locations using the harmonic mean of thermal conductivity and temperature gradient specific to each borehole.

$$q_s = -K_t \times \frac{dT}{dZ} \quad (3)$$

Where q_s means the heat flow, measured in mW/m^2; K_t represents the harmonic mean value of thermal conductivity, expressed in W/(m·K); dT/dZ stands for the geothermal gradient, in ℃/m.

The results show that the surface heat flow in the Junggar Basin ranging from 32.7 mW/m^2 to 68.5 mW/m^2, with an average of 45.8 mW/m^2 (Fig. 8). In the uplifted regions, heat flow exceeds 44 mW/m^2. while depression zones have lower values, below 44 mW/m^2. Compared to other Chinese basins, the Junggar Basin's heat flow aligns closely with

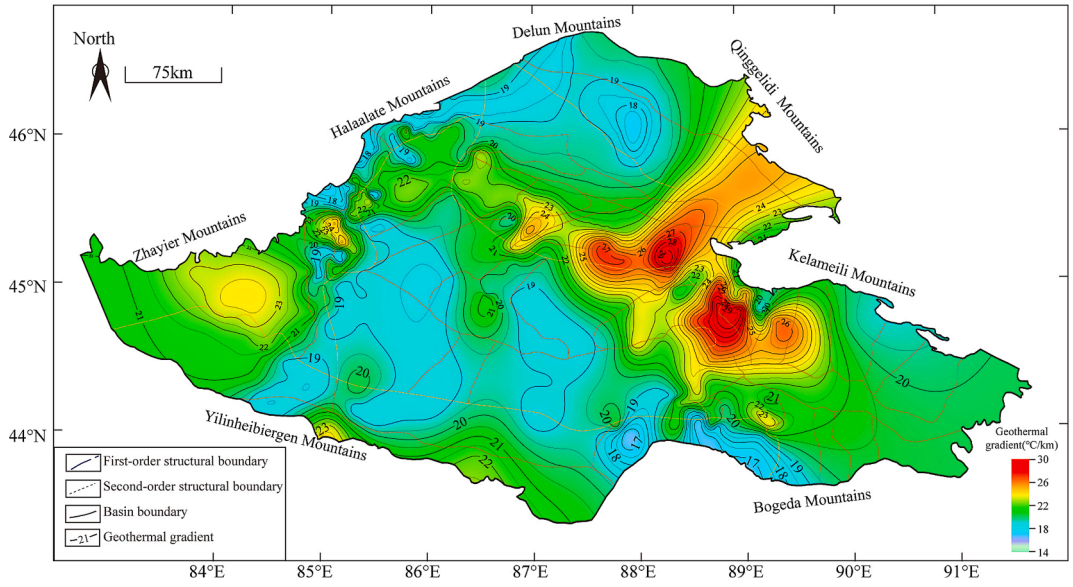

Fig. 7. The distribution of geothermal gradient at the uniform depth of 4000 m in the Junggar Basin.

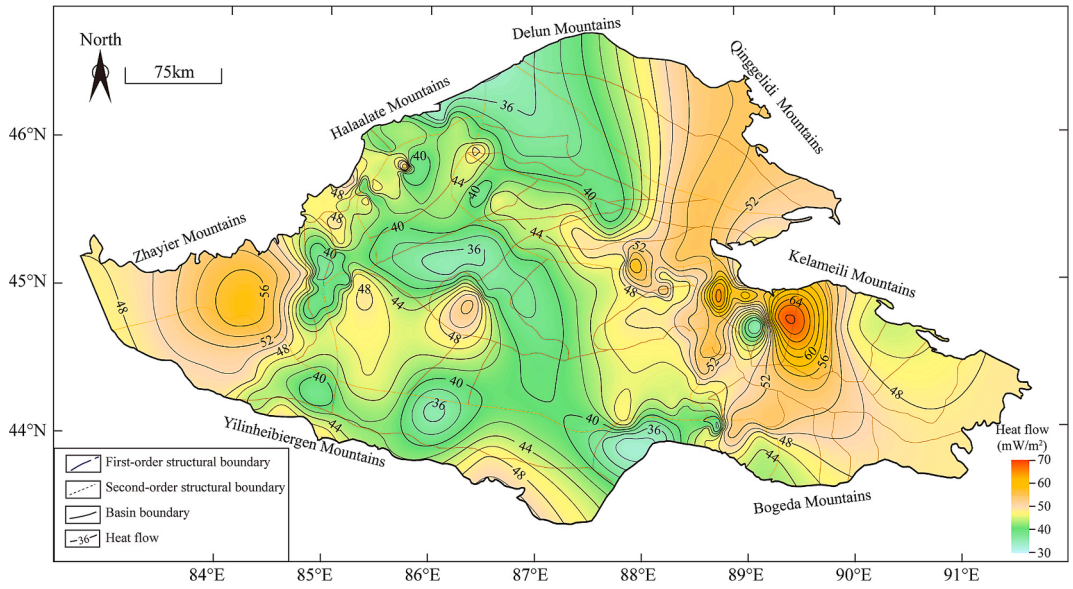

Fig. 8. The distribution of heat flow in the Junggar Basin.

the Tarim Craton Basin, averaging approximately 42.5 mW/m^2, However, it is lower than that of the medium and large sedimentary basins in central, eastern, and offshore China. This heat flow is also consistent with corresponding values in the Siberian, Michigan, and Murzuq basins, which are all lower than 50 mW/m^2 (Liu et al., 2020), indicating the basin's stable tectonic setting of the Junggar Basin and its typical low geothermal background.

Spatial variation in heat flow within the Junggar Basin shows that the eastern uplift has the highest average heat flow at 50.5 mW/m^2, while the Wulugu Depression, Luliang Uplift, and Western Uplift show intermediate averages of 48.2, 47.7, and 46.3 mW/m^2, respectively. The Southern Overthrust Belt and Central Depression have lower averages, at 44.4 mW/m^2 and 42.9 mW/m^2 respectively (Fig. 8).

3.4. The distribution characteristics of deep formation temperature

Deep formation temperature is critical for guiding future exploration of hydrocarbon and geothermal resources. However, since most wells in the Junggar Basin are completed at depths less than 6000 m, direct measurement of deeper formation temperatures is not feasible. This study addresses this challenge by estimating ultradeep temperatures (5000–10000 m) using data from shallower formations. By integrating collected temperature data, thermal property parameters, and sedimentary layer thicknesses, we applied Equation (1) to calculate temperatures at these depths. Validation against measured temperatures from wells exceeding 5000 m shows a deviation of less than 3℃, demonstrating the reliability of the estimation method (Figs. 4 and 5).

The results indicate that deep formation temperatures range from 84.4℃ at 5000 m to 311.5℃ at 10000 m, with consistent trends reflecting the geothermal gradient in the Junggar Basin (Table 3, Fig. 9Uplift areas generally exhibit higher temperatures at the same depth, while depression zones show lower temperatures. Some anomalies were observed, such as the western uplift of the Wulungu Depression being cooler than the eastern uplift, the northwestern uplift areas having lower temperatures than other uplifts, and the southern margin depression areas showing higher temperatures compared to other depressions. In the Southern Overthrust Belt, temperatures decrease progressively from the piedmont toward the basin interior (Fig. 9).

4. The structures and thickness of thermal lithosphere

The thermal lithosphere's structure refers to the distribution and interaction of heat flow, which consists of two primary components: crustal heat flow, generated by the radioactive decay of elements such as uranium (U), thorium (Th), and potassium (K) in the crust; and mantle heat flow, originating from deeper within the mantle (Blackwell, 1971). Mantle heat flow is theoretically estimated through a linear relationship between the thermal properties of rocks. However, this relationship often breaks down in sedimentary basins. To address this limitation, Wang et al. (1986) proposed a "back-stripping" method that calculates mantle heat flow in sedimentary basins by incorporating surface heat flow, heat generation rates, and crustal thickness (Equation (4)).

$$q_m = q_s - q_c = q_s - \Sigma A_i D_i \tag{4}$$

Here, mantle heat flow (q_m, mW/m^2) is derived as a function of: surface heat flow (q_s, mW/m^2), the total heat flow at the earth's surface, crustal heat flow (q_c, mW/m^2), from radioactive decay in the crust, Thickness of the crustal layer (D_i, km), and radioactive heat production rate (A_i, μW/m^3).

For the Junggar Basin, tectonic units were defined following Shao et al. (2008). Shallow thermal conductivity was measured in this study, while data for deep conductivity and heat generation rates were drawn

Table 3
Formation temperature at depths of 5000–10000m in the Junggar Basin.

Tectonic Unit	T5000m (℃)	T6000m (℃)	T7000m (℃)	T8000m (℃)	T9000m (℃)	T10000m (℃)
Eastern uplift	121.3 (99.8-162.4)	142.8 (117.1-192.2)	164.4 (134.3-222.1)	187.3 (151.6-250.9)	207.5 (168.8-281.7)	229.1 (186.1-311.5)
Southern Overthrust Belt	114.3 (96.1-132.3)	134.5 (112.6-156.1)	154.6 (129.1-179.9)	174.7 (145.8-201.4)	194.9 (162.1-227.4)	215.1 (178.5-251.2)
Western	117.8 (84.4-138.1)	138.6 (98.5-162.9)	159.5 (112.8-187.1)	180.3 (125.7-212.4)	201.2 (140.9-237.6)	221.9 (155.1-262.5)
Central Depression	110.9 (99.4-154.2)	130.4 (116.6-182.4)	149.9 (133.8-210.5)	168.9 (150.9-238.9)	188.82 (168.1-266.8)	208.3 (185.3-295.1)
Luliang Uplift	118.8 (91.1-161.5)	139.8 (106.5-191.1)	160.9 (121.9-220.7)	181.8 (136.2-246.8)	202.9 (152.9-279.9)	223.9 (163.3-309.6)
Wulungu Depression	117.9 (95. 3-141.2)	138.8 (111.7-166.7)	159.7(127.9-192.3)	180.3(142.8-215.9)	201.4 (160.7-243.3)	222.3 (176.9-268.9)

Note: T means the formation temperature, The data is the average temperature and temperature range at different depths.

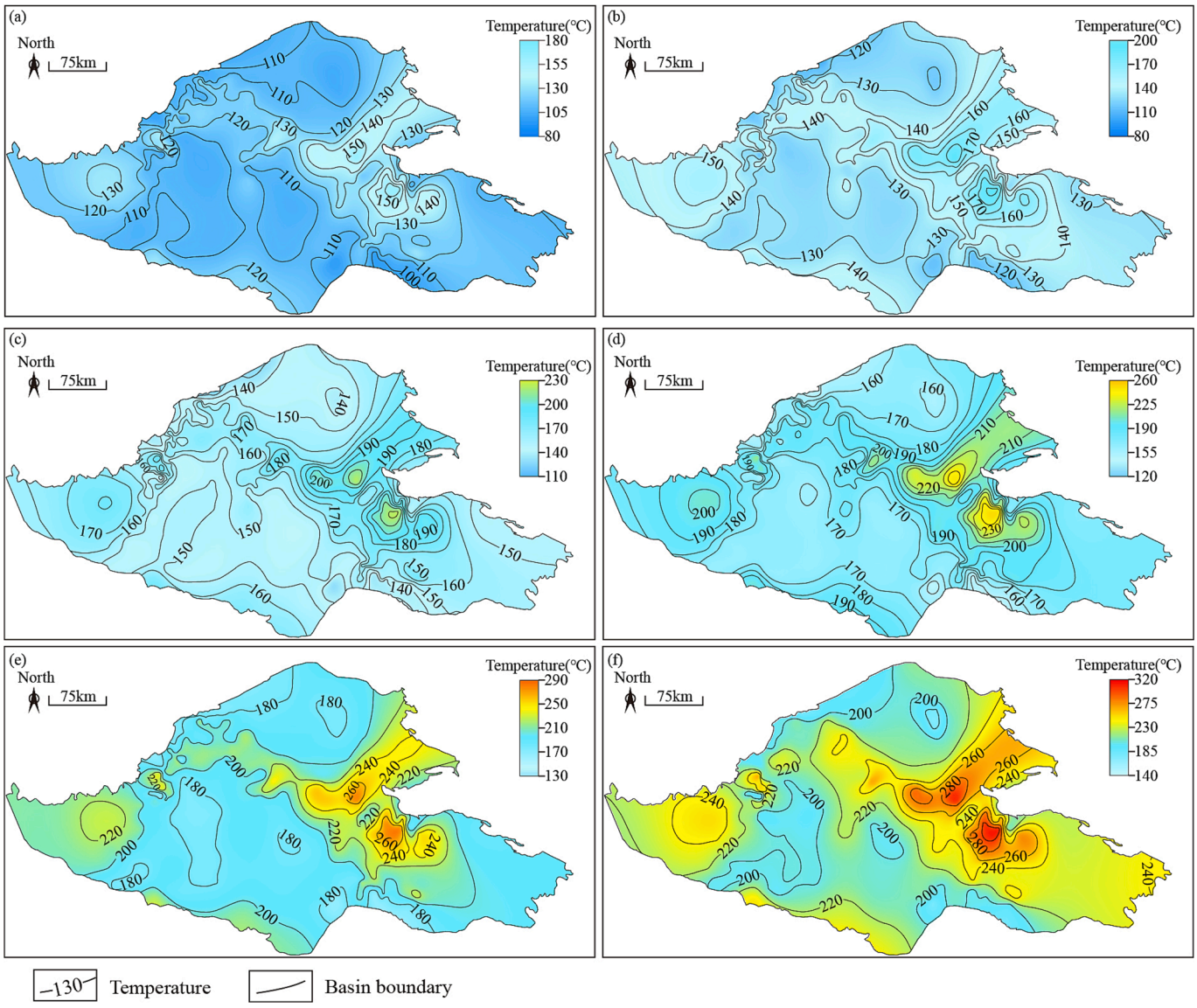

Fig. 9. Temperature distribution of 5000 m (a), 6000 m (b), 7000 m (c), 8000 m (d), 9000 m (e) and 10000 m (f) in the Junggar Basin.

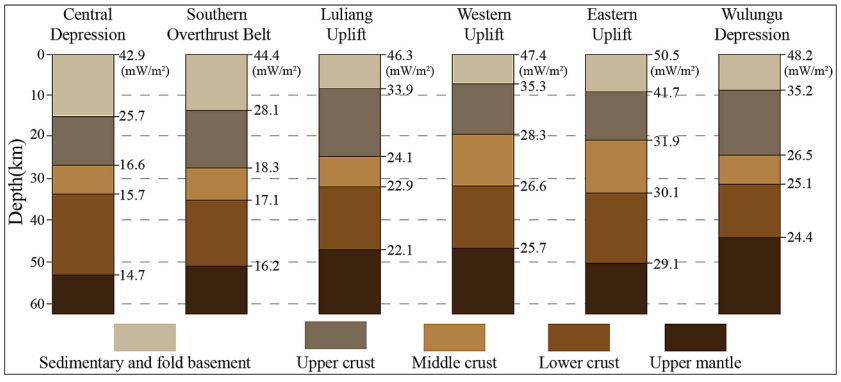

Fig. 10. Heat flow calculated results of tectonic layers in Junggar Basin.

from earlier work (Qiu, 2002; Rao et al., 2013). The crust-to-mantle heat flow ratio ranges from 0.74 to 1.92, reflecting a cold crust and mantle structure. This detailed heat flow analysis refines previous studies, which estimated the crust-to-mantle heat flow ratio broadly at 0.79–1.58, based on average surface heat flow (Rao et al., 2013). The findings also align with the mantle heat flow of 21 mW/m^2 and crust-mantle heat flow ratio of 1.5 derived from subsurface fluid analysis (Wang, 2000).

The thermal lithosphere is the portion of the lithosphere where heat transfer is dominated by conduction, with its lower boundary marked by

the transition to the convecting asthenosphere. A depth-temperature profile of the lithosphere, calculated using Equation (1), defines the thermal lithosphere's upper and lower boundaries at the intersections of the profile with mantle adiabatic lines, as described in Equations (5) and (6) (Artemieva and Mooney, 2001).

$$T_1 = 1200 + 0.5 \times Z \quad (5)$$

$$T_2 = 1300 + 0.4 \times Z \quad (6)$$

The present-day thermal lithosphere thickness in the Junggar Basin ranges from 143 to 291 km, approximately 10 km thinner than the seismic lithosphere (Zhi et al., 2018). Uplifted areas show thinner lithosphere (143–179 km), while the Central Depression and Southern Overthrust Belt exhibit greater thicknesses of 260 km and 291 km, respectively (Fig. 11).

5. Discussion

5.1. Primary determinants of the geothermal regime

The geothermal regime in the Junggar Basin exhibits a pattern of lower heat flow in depressions and higher values in uplifts. Terrestrial heat flow increases from the basin center toward its periphery, primarily driven by variations in the burial depth of the folded basement, which ranges from 5 to 16 km (Fig. 12; Qu et al., 2008; Shao et al., 2008). Composed of granite and metamorphic rocks with high thermal conductivity and heat generation rates, the folded basement significantly contributes to surface heat flow. In the Central Depression and Southern Overthrust Belt, the folded basement is buried at depths of 6–16 km, while in the Eastern Uplift, Luliang Uplift, Wulungu Depression, and most of the Western Uplift, it lies at depths of less than 6 km with relatively thinner sedimentary layers. The low thermal conductivity of these sedimentary layers restricts upward heat transfer, resulting in lower heat flow in the Central Depression and Southern Overthrust Belt compared to the higher values observed in uplifted regions.

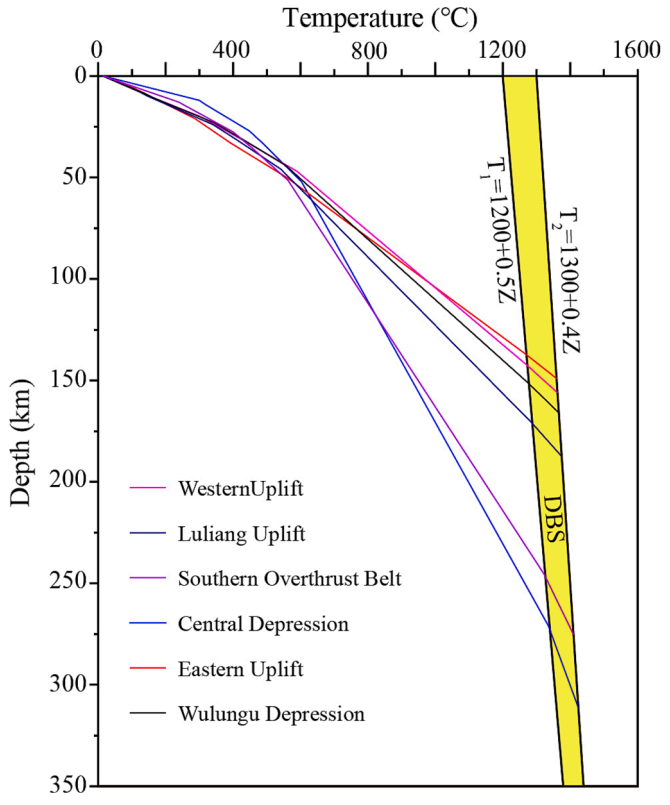

Fig. 11. Calculated thermal lithosphere thickness in the Junggar basin. DBS stands for Dry Basalt Solidus line. The base of the thermal lithosphere is defined as the intersection of the model geotherm with the DBS.

The geothermal characteristics of the basin are also influenced by the spatial distribution and lithological composition of volcanic rocks (Fig. 13). In the Luliang Uplift and Wulungu Depression, despite minimal differences in basement burial depth, heat flow displays a distinct west-to-east gradient, with lower values in the west and higher values in the east. This variation correlates with differences in basement lithology and magmatic activity. The Wulungu Depression is dominated by mafic rocks, while the Luliang Uplift features intermediate and felsic rocks, which generate more heat (Wang et al., 2019; Wu et al., 2008; Zhou et al., 2006). Additionally, magmatic activity in the west occurred primarily during the Carboniferous and Permian periods, with limited outcrop exposure. In contrast, the eastern region experienced more intense Devonian volcanic activity, resulting in higher heat flow in the eastern Luliang Uplift (Wu et al., 2008; Wu et al., 2009).

Interestingly, areas along the southern margin of the Southern Overthrust Belt, where the folded basement is deeply buried adjacent to orogenic belts, exhibit higher heat flow—a finding that contrasts with previous studies (Rao et al., 2013; Wang et al., 2000; Qiu et al., 2001; Zhang et al., 2024). Fault activity significantly impacts the geothermal regime through two mechanisms: temperature changes due to strain and frictional heating from fault displacement (Wang et al., 2003). While strain-induced temperature increases are minor and gradual, frictional heating leads to substantial temperature rises, particularly near fault zones. Larger fault displacements and proximity to fault zones amplify this effect (Baietto et al., 2008).

The southern margin of the Junggar Basin underwent two tectonic deformation phases during the Late Jurassic and Miocene. Thermal anomalies associated with Late Jurassic fault activity are unlikely to persist to the present and thus do not influence the current geothermal field. However, Cenozoic thrust nappe tectonics caused intense deformation in the Tianshan piedmont region. These relatively recent tectonic events led to frictional heating from fault displacement, elevating geothermal temperatures in the area (Zhou et al., 2020). Orogenic processes in the Northern Tianshan Orogenic Belt have also produced reverse faults along the basin's southern margins (Chang et al., 2022; Charreau et al., 2008; Lu et al., 2010; Peng et al., 2024). These faults act as conduits for deep heat transfer, contributing to higher heat flow along the northern basin margin.

5.2. Relationship between the thermal structure of the lithosphere and the basin's tectonic background

The Junggar Basin is characterized as a cold basin with a cold mantle and crust, as reflected by its low heat flow (<50 mW/m^2) and a crust-to-mantle heat flow ratio of 0.74–1.92 (Fig. 10). Studies on the thermal structure of lithospheres across China reveal a consistent decrease in mantle heat flow from east to west. In tectonically active regions like the Mesozoic-Cenozoic rift basins of eastern China, much of the heat originates from the mantle (Wang et al., 2023). In contrast, stable regions such as the western cratons of China show minimal heat contribution from deep sources.

In the Junggar Basin, the thermal structure and temperature distribution of the lithosphere are highly heterogeneous. Temperature generally increases with depth but varies significantly between the central depression and surrounding uplifts. The thickness of the thermal lithosphere is also uneven. Pollack et al. (1993) provide heat flow benchmarks for different geological eras: Archean (41 ± 2.4 mW/m^2), Proterozoic (58 ± 1.4 mW/m^2), Paleozoic (58–61 mW/m^2), Mesozoic (64 ± 3.0 mW/m^2), and Cenozoic (64–97 mW/m^2). Comparing these values with those of Junggar Basin's tectonic units reveals that the central and southern depression zones, classified as stable regions, have not been significantly influenced by Cenozoic thermal events. Conversely, the Altai and Tianshan orogenic belts, affected by tectonic activity from the India-Asia plate collision, exhibit higher heat flow due

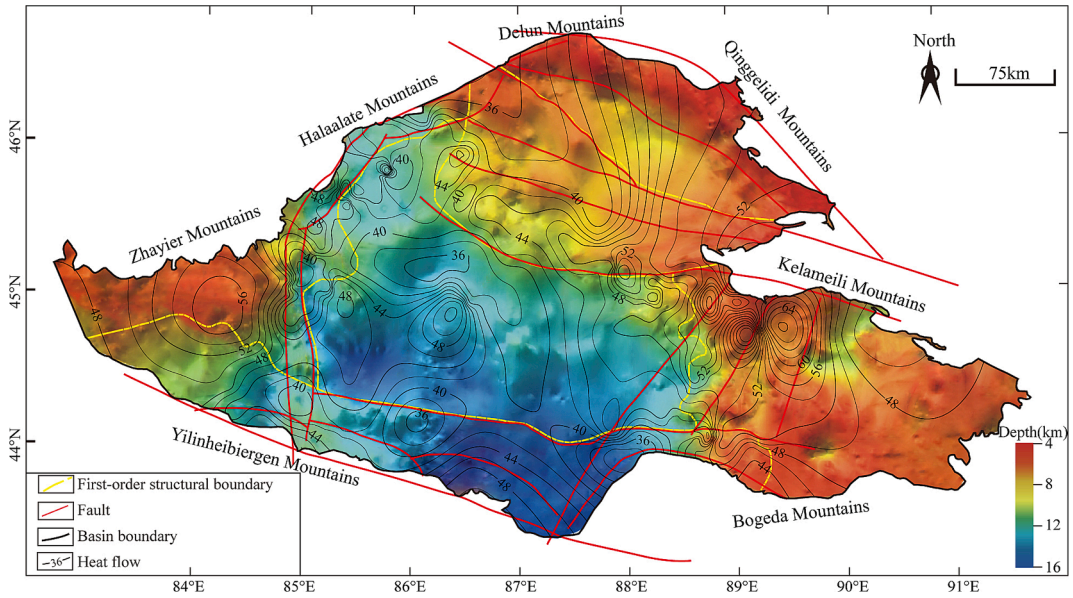

Fig. 12. The depth of the folded basement and the fault distribution in Junggar Basin (modified after Qu et al.(2008)).

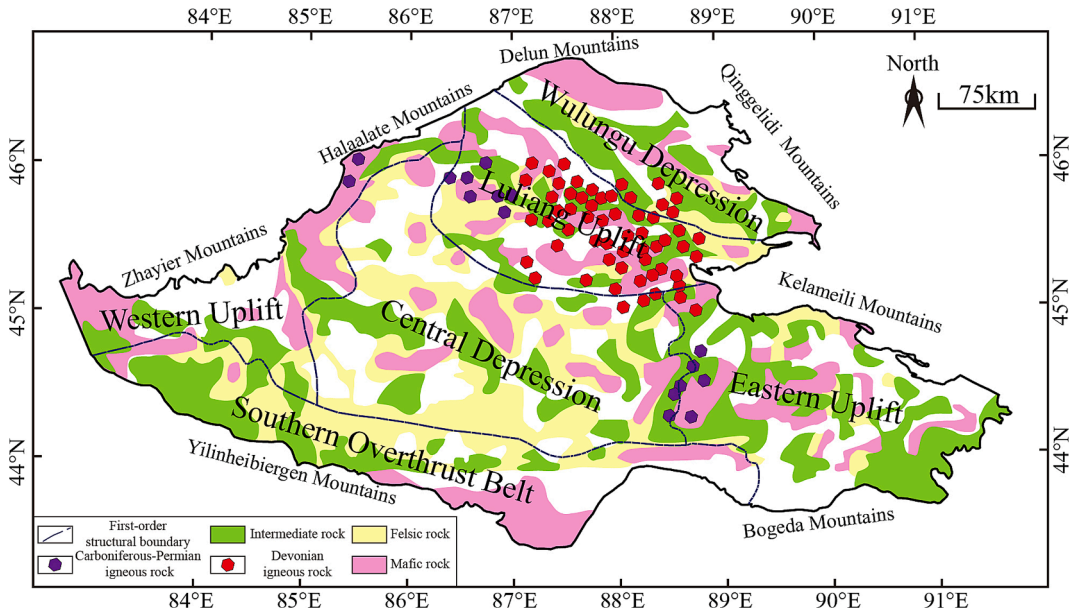

Fig. 13. The lithology and distribution of basement igneous rocks in the Junggar Basin, and the locations of Devonia-Permian volcanic activity (modified after Mao et al. (2012)).

to ongoing tectonic processes (Wang et al., 2003).

The basin's geothermal characteristics are closely linked to its tectonic evolution, which spans several major phases: Paleozoic and Mesozoic collision and amalgamation of ancient landmasses, coupled with volcanic activity and tectonic reworking; rift basin formation under extensional conditions during the Carboniferous-Permian; intracontinental depression basin development during the Mesozoic; and foreland basin formation under compressional conditions during the Cenozoic (He et al., 2018). These phases reflect a transition from a high-heat to a low-heat thermal background. Extensive volcanic activity during the Carboniferous created a hot geothermal environment (Qiu, 2002). Over time, internal heat flow decreased, with the high heat flow from the Carboniferous-Permian rifting stage no longer influencing the present thermal regime.

Tectonic subsidence analysis reveals that the Junggar Basin experienced slow subsidence during the Paleogene, followed by rapid subsidence from the Neogene to the Quaternary. This rapid subsidence, unlike the rifting-driven subsidence of the Carboniferous-Permian, was caused by northward compressional forces from the Indian plate. These forces uplifted the Tianshan Mountains along the basin's southern margin, inducing thrusting into the basin and rapid flexural subsidence. This process corresponded to lithospheric thickening and cooling, in contrast to the lithospheric thinning and heating associated with the rift stage (He et al., 2018). The basin's overall low thermal background can be attributed to its stable Precambrian crystalline basement and the rapid accumulation of cold sediments during the late Cenozoic foreland basin phase. From the Paleogene to the Quaternary, tectonic activity—dominated by flexure, shallow thrusting, and lithospheric thickening—further reinforced the cold thermal regime, reflecting the basin's post-Mesozoic tectono-thermal evolution.

5.3. Impact of the formation temperature on the hydrocarbon phase state and geothermal resource

Formation temperature is a critical factor influencing hydrocarbon generation and cracking depths (Barker and Pawlewicz, 1986). When comparing across various basins, those with lower geothermal gradients demonstrate deeper burial depths for isotherms representing specific temperatures (Ren et al., 2020). For example, in basins with varying geothermal conditions, the depth ranges for the oil window (65–165℃), oil cracking (165–200℃), and complete cracking (>240℃) increase progressively with depth (Lu and Xue, 2002; Price, 1993; Waples, 2000). In the Junggar Basin, source rocks are concentrated in the central region (Fig. 14). Due to differential burial depths, these rocks exhibit varied maturation levels over geological time (He et al., 2019). Oil and gas fields in the basin's northwest margin reveal contrasting heat flow conditions: oil fields typically have heat flow below 45 mW/m^2, while gas fields exhibit heat flow above 45 mW/m^2, indicating that higher geothermal gradients accelerate source rock maturation.

Deep and ultra-deep formation temperatures in the Junggar Basin increase from the central region to the margins (Figs. 9 and 15). At 8000 m depth in the central basin, temperatures remain below 160℃, enabling liquid oil preservation. Condensate gas reservoirs are found between 8000 and 10000 m, while dry gas reservoirs occur beyond 10000 m. In contrast, at the high-temperature basin margins, liquid oil preservation is limited to depths shallower than 6000 m. Comparatively, basins in eastern China show shallower hydrocarbon preservation depths: liquid oil below 5000 m, condensate gas between 5000 and 6000 m, and dry gas reservoirs at shallower depths (Ren et al., 2020).

Formation temperature also determines geothermal resource potential, classified as low-temperature (25–90℃), medium-temperature (90–150℃), and high-temperature (>150℃) resources (Wang et al., 2015). The eastern uplift area of the Junggar Basin, with high heat flow, exhibits formation temperatures above 150℃ at 5000 m, indicating potential for high-temperature geothermal resources. In the central basin, lower heat flow results in medium-temperature geothermal resources at 5000 m and high-temperature resources at 7000 m (Fig. 15). In summary, the low geothermal regime in the central Junggar Basin favors hydrocarbon preservation, offering significant potential for exploration. Conversely, the eastern uplift's higher heat flow suggests strong prospects for geothermal resource development.

6. Conclusion

This study systematically analyzed the geothermal regime of the Junggar Basin and evaluated the resource potential of its deep and ultra-deep formations. The basin's geothermal gradient and heat flow range from 14.0 to 29.8℃/km and 32.7–68.5 mW/m^2, respectively, with mean values 20.7 ℃/km and 45.8 mW/m^2. The crust–mantle heat flow ratio spans 0.74–1.92 and the thermal lithosphere thickness varies from 150 to 270 km across tectonic units. These findings confirm the Junggar Basin's cold geothermal background and stable tectonic state. The geothermal regime is primarily influenced by folded basement relief, with local variations linked to basement lithology and fault activity. Formation temperatures at 10 km depths range from 155 to 311℃, reflecting significant contrasts between depressions and uplifts. Liquid oil is preserved at depths of 8000 m in the central basin, while gas resources are found at depths shallower than 6000 m in the Eastern Uplift. Additionally, the eastern uplift region, with formation temperatures exceeding 150℃ at 5000 m, shows strong potential for high-temperature geothermal resource development.

CRediT authorship contribution statement

Chenxing Li: Writing – original draft, Visualization, Validation, Software, Methodology, Data curation. **Jian Chang:** Writing – review & editing, Visualization, Supervision, Project administration, Conceptualization. **Nansheng Qiu:** Supervision, Project administration, Conceptualization. **Huajun Guo:** Project administration, Funding acquisition, Conceptualization. **Xiang Shan:** Resources, Formal analysis. **Bo Peng:** Methodology, Funding acquisition, Data curation. **Jiabo Xu:** Validation, Software, Methodology, Data curation. **Ze Zhang:** Validation, Software, Formal analysis.

Declaration of competing interest

The authors declare that they have no known competing financial

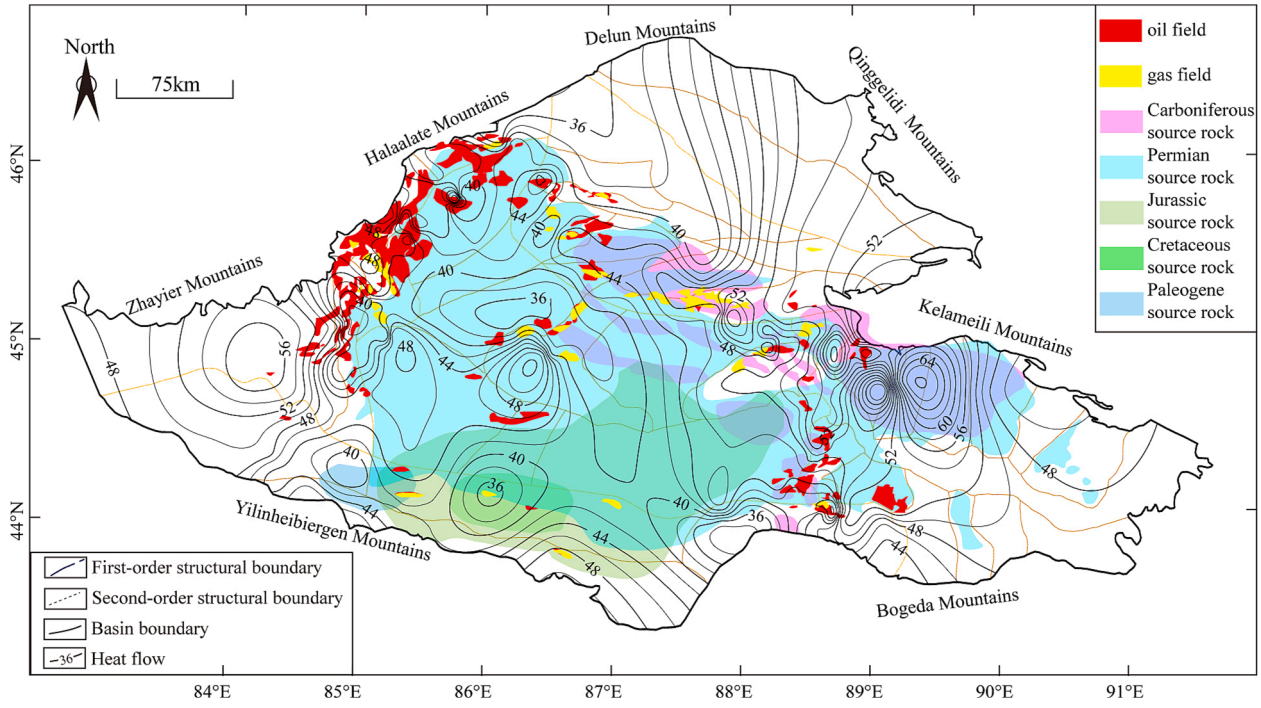

Fig. 14. Heat flow, oil and gas field and and source rock location in the Junggar Basin (modified after He et al. (2019) and Tang et al. (2022)).

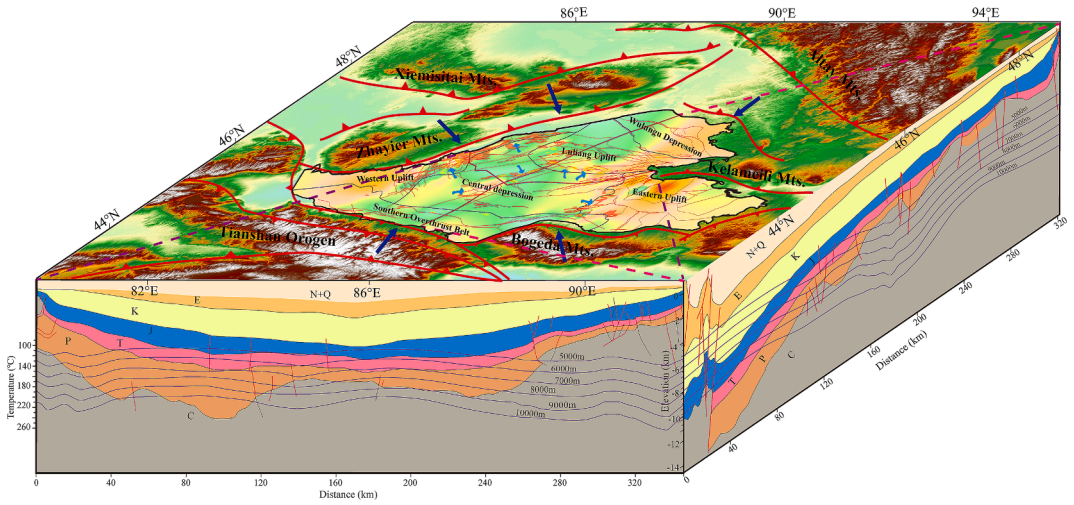

Fig. 15. Geothermal regime model of the Junggar Basin. The topographic contour is based on Digital Elevation Model data. Red lines indicate fractures, dark blue arrows represent mountain range compression directions, and light blue arrows show oil and gas accumulation directions. The cross-sectional diagram illustrates the vertical distribution of sedimentary layer depths and temperatures.

interests or personal relationships that could have appeared to influence the work reported in this paper.

Acknowledgements

This work was funded by the China National Petroleum Corporation's Important Science and Technology Project (No. 2023ZZ24-01) and the China National Petroleum Corporation's "Fourteenth Five Year Plan" Basic Prospective Major Scientific and Technological Projects (No. 2021DJ0202 and No.2021DJ0108).

Data availability

Data will be made available on request.

References

Baietto, A., Cadoppi, P., Martinotti, G., Perello, P., Perrochet, P., Vuataz, F.D., 2008. Assessment of thermal circulations in strike-slip fault systems: the Terme di Valdieri case (Italian western Alps). Geol. Soc. Lond. Spec. Publ. 299, 317–339.

Barker, C.E., Pawlewicz, M.J., 1986. The correlation of vitrinite reflectance with maximum temperature in humic organic matter. In: Buntebarth, G., Stegena, L. (Eds.), Paleogeothermics: Evaluation of Geothermal Conditions in the Geological past. Springer Berlin Heidelberg, Berlin, Heidelberg, pp. 79–93.

Artemieva, I.M., Mooney, W.D., 2001. Thermal thickness and evolution of Precambrian lithosphere: A global study. J. Geophys. Res. Solid Earth 106, 16387–16414.

Blackwell, D.D., 1971. The thermal structure of the continental crust. The Structure and Physical Properties of the Earth's Crust 14, 169–184.

Chang, J., Li, D., Qiu, N., Zhu, C., Zhong, N., Feng, Q., Zhang, H., Wang, X., 2022. Differential Thermal Regimes of the Tarim and Sichuan Basins in China: Implications for Hydrocarbon Generation and Conservation. Acta Geologica Sinica - English Edition 96, 1308–1322.

Chang, J., Qiu, N., Zhao, X., Xu, W., Xu, Q., Jin, F., Han, C., Ma, X., Dong, X., Liang, X., 2016. Present-day geothermal regime of the Jizhong depression in Bohai Bay basin, East China. Chinese Journal of Geophysics (in Chinese) 59, 1003–1016.

Charreau, J., Avouac, J.-P., Chen, Y., Dominguez, S., Gilder, S., 2008. Miocene to present kinematics of fault-bend folding across the Huerguosi anticline, northern Tianshan (China), derived from structural, seismic, and magnetostratigraphic data. Geology 36, 871–874.

Fang, S., Guo, Z., Jia, C., Zhang, Z., Wang, X., Wang, M., 2006. Meso-Cenozoic Heavy Minerals' Assemblages in the Southern Junggar Basin and its Implications for Basin-Orogen Pattern. Chinese Journal of Geology 41, 648–662.

Gu, Y., Wan, Y., Huang, J., Zhuang, X., Wang, B., Li, M., 2019. Prospects for ultra-deep oil and gas in the "deep burial and high pressure" Tarim Basin. Pet. Geol. Exp. 41, 157–164.

Guan, X., Wu, C., Xu, Y., Jolivet, M., Xiu, J., Lin, C., 2024. A fluvial-aeolian system in response to aridification during the Late Mesozoic, Junggar Basin. Central Asia. Basin Research 36, e12879.

He, D., Zhai, G., Kuang, J., Zhang, Y., Shi, X., 2005. Distribution and tectonic features of paleo-uplifts in the Junggar Basin. Chinese Journal of Geology 40, 248–261.

He, D., Zhang, L., Wu, S., Li, D., Zhen, Y., 2018. Tectonic evolution stages and features of the Junggar Basin. Oil Gas Geol. 39, 845–861.

He, W., Fei, L., Yiming, A., Yang, H., Lan, W., Ding, J., Bao, H., Guo, W., 2019. Accumulation conditions of deep hydrocarbon and exploration potential analysis in Junggar Basin, NW China. Earth Sci. Front. 26, 189–201.

Jia, C., Pang, X., 2015. Research processes and main development directions of deep hydrocarbon geological theories. Acta Pet. Sin. 36, 1457.

Jin, J., Liu, M., Liu, Y., Wang, J., Gao, C., Luo, F., Ren, Y., 2021. Present-day temperature-pressure field and its controlling factors of the lower composite in the southern margin of Junggar Basin. Chinese Journal of Geology 56, 28–43.

Kämmlein, M., Stollhofen, H., 2019. Lithology-specific influence of particle size distribution and mineralogical composition on thermal conductivity measurements of rock fragments. Geothermics 80, 119–128.

Liu, Y., Qiu, N., Li, H., Ma, A., Chang, J., Jia, J., 2020. Terrestrial heat flow and crustal thermal structure in the northern slope of Tazhong uplift in Tarim Basin. Geothermics 83, 101709.

Lu, H., Burbank, D.W., Li, Y., Liu, Y., 2010. Late Cenozoic structural and stratigraphic evolution of the northern Chinese Tian Shan foreland. Basin Res. 22, 249–269.

Ren, Z., Cui, J., Qi, K., Yang, G., Chen, Z., Yang, P., Wang, K., 2020. Control effects of temperature and thermal evolution history of deep and ultra-deep layers on hydrocarbon phase state and hydrocarbon generation history. Nat. Gas Ind. B 7, 453–461.

Mao, X., Li, J., Zhang, H., Wang, L., 2012. Study on the distribution and developmental environment of the Late Paleozoic volcanoes in Junggar Basin and its adjacent areas. Acta Petrol. Sin. 28, 2381–2391.

Peng, Z., Graveleau, F., Vendeville, B.C., Wang, X., Averbuch, O., 2024. Interaction between basement inherited strike-slip structures and thrust wedge propagation in the northern Tianshan foreland basin: Insight from analogue modelling experiments. J. Struct. Geol. 183, 105143.

Pollack, H.N., Hurter, S.J., Johnson, J.R., 1993. Heat flow from the Earth's interior: analysis of the global data set. Rev. Geophys. 31, 267–280.

Popov, Y.A., Pribnow, D.F.C., Sass, J.H., Williams, C.F., Burkhardt, H., 1999. Characterization of rock thermal conductivity by high-resolution optical scanning. Geothermics 28, 253–276.

Price, L.C., 1993. Thermal stability of hydrocarbons in nature: limits, evidence, characteristics, and possible controls. Geochim. Cosmochim. Acta 57, 3261–3280.

Qiu, N., 2002. Characters of thermal conductivity and radiogenic heat production rate in basins of northwest China. Chinese Journal of Geology 37, 196–206.

Qiu, N., Wang, X., Yang, H., Xiang, Y., 2001. The characteristics of temperature distribution in the Junggar Basin. Chinese Journal of Geology 36, 350–358.

Qu, G., Ma, Z., Shao, X., Zhang, X., 2008. Basements and crust structures in Junggar Basin. Xinjiang Petroleum Geology 29, 669.

Rao, S., Hu, S., Zhu, C., Tang, X., Li, W., Wang, J., 2013. The characteristics of heat flow and lithospheric thermal structure in Junggar Basin, northwest China. Chin. J. Geophys. 56, 2760–2770.

Ren, Z., Zhang, S., Gao, S., Cui, J., Xiao, Y., Xiao, H., 2007. Tectonic thermal history and its significance on the formation of oil and gas accumulation and mineral deposit in Ordos Basin. Sci China Ser D Earth Sci 50, 27–38.

Song, J., Wang, G., Xing, L., Qian, J., Dai, L., Di, H., 2023. Influencing factors of rock thermal conductivity and applicability evaluation of its mixing law predictive models. Geothermics 110, 102680.

Shao, X., Zhang, J., Huiji, F., Romahov, U., Kaydash, F., 2008. The basement structure in Junggar basin: deep-sounding by converted waves of earthquakes. Xinjiang Petroleum Geology 29, 439.

Tang, Y., Song, Y., He, W., Zhao, L., Yang, H., Zhao, C., Zheng, M., Sun, S., Fei, L., 2022. Characteristics of composite hydrocarbon accumulation in a superimposed basin, Junggar Basin. Oil Gas Geol. 43, 132–148.
Wang, G., Liu, Y., Duan, H., Liu, Z., Hu, J., Bian, K., Xing, L., 2023. Crust-mantle differentiation and thermal accumulation mechanisms in the north China plain. Renew. Energy 213, 63–74.
Wang, J., 2015. Geothermal and its application. Science Press, Beijing.
Wang, J., Wang, J., Yan, S., Lu, X., 1986. Geothermal studies in oil field districts of North China. In: Buntebarth, G., Stegena, L. (Eds.), Paleogeothermics: Evaluation of Geothermal Conditions in the Geological past. Springer Berlin Heidelberg, Berlin, Heidelberg, pp. 195–204.
Wang, L., Li, C., Liu, S., Li, H., Xu, M., Wang, Q., Ge, R., Jia, C., Wei, G., 2003. Geotemperature gradient distribution of Kuqa foreland basin, North of Tarim, China. Chin. J. Geophys. 46, 403–407.
Wang, L., Li, Y., Wang, Z., Ning, W., Tao, X., Xu, Q., 2019. Zircon LA-ICP-MS U-Pb Dating of Volcanics in Batamayineishan Formation of Kalamaili Area, Eastern Junggar. Xinjiang Geol. 37, 44–50.
Wang, S., He, L., Wang, J., 2001. Thermal regime and petroleum systems in Junggar basin, northwest China. Phys. Earth Planet. In. 126, 237–248.
Wang, S., Hu, S., Wang, J., 2000. The characteristics of heat flow and geothermal field in Junggar Basin. Chin. J. Geophys. 43, 816–824.
Wang, Y., 2000. Estimations of the ratio of crust/mantle heat flow using Helium isotope ratio of underground fluid. Acta Geophys. Sin. 43, 762–770.
Waples, D.W., 2000. The kinetics of in-reservoir oil destruction and gas formation: constraints from experimental and empirical data, and from thermodynamics. Org Geochem. 31, 553–575.
Wu, X., Liu, D., Wei, G., Li, J., Li, Z., 2009. Geochemical characteristics and tectonic settings of Carboniferous volcanic rocks from Ludong-Wucaiwan area, Junggar basin. Acta Petrol. Sin. 25, 55–66.
Wu, X., Qi, X., Tang, Y., Wei, Y., Hou, L., 2008. Carboniferous strata and lithofacies paleogeography & source rock in northern Xinjiang. Geoscience 22, 549.
Wu, Y., Liu, C., Jiang, F., Hu, T., Lv, J., Zhang, C., Guo, X., Huang, L., Hu, M., Huang, R., 2022. Geological characteristics and shale oil potential of alkaline lacustrine source rock in Fengcheng Formation of the Mahu Sag, Junggar Basin, Western China. J. Pet. Sci. Eng. 216, 110823.
Zhang, C., Wang, F., Zhang, Y., Lu, H., Zhang, H., Huang, R., Liu, Z., Chen, J., 2024. An updated terrestrial heat flow data set for the Junggar basin, northwest China: implications for geothermal resources. Geophys. J. Int. 239, 1103–1116.
Zhi, J., Du, J., Chen, C., 2018. Characteristics of Large-Scale Thermal Structure in Lithosphere beneath Junggar Basin and Surroundings. Earth Sci. 43, 103–118.
Zhou, T., Yuan, F., Yang, W., He, L., Tan, L., Fan, Y., Yue, S., 2006. Permian volcanism in the Sawu'er area, western Junggar. Geol. China 33, 553–558.
Zhou, X., Wang, X., Chen, W., Yu, Y., Meng, L., 2020. Structural deformation and transition relations of the deep structure in the central margin of the southern Junggar Basin. Chinese Journal of Geology 55, 339–351.
Zhou, Y., Fu, A., Zhao, X., 2024. Jurassic Source Rock Characteristics and Resource Evaluation in Junggar Basin. International Journal of Natural Resources and Environmental Studies 3, 54–59.